Since January 2020 Elsevier has created a COVID-19 resource centre with free information in English and Mandarin on the novel coronavirus COVID-19. The COVID-19 resource centre is hosted on Elsevier Connect, the company's public news and information website.

Spectrochimica Acta Part A: Molecular and Biomolecular Spectroscopy 261 (2021) 120006

Contents lists available at ScienceDirect

Spectrochimica Acta Part A: Molecular and Biomolecular Spectroscopy

journal homepage: www.elsevier.com/locate/saa

Computational details of molecular structure, spectroscopic properties, topological studies and SARS-Cov-2 enzyme molecular docking simulation of substituted triazolo pyrimidine thione heterocycles

Doaa S. El Sayed [a,*], El-sayed M. Abdelrehim [b]

[a] Chemistry Department, Faculty of Science, Alexandria University, Alexandria, Egypt
[b] Chemistry department, Faculty of science, Damanhour University, Damanhur, Egypt

HIGHLIGHTS

- The electronic properties of some heterocyclic derivatives were studied and discussed based on DFT calculations.
- Estimation the quantum chemical parameters and topological analyses provided analyzing picture about the active sites of the molecular structure.
- Molecular docking was applied on the viral enzymatic SARS-Cov-2 protein.

GRAPHICAL ABSTRACT

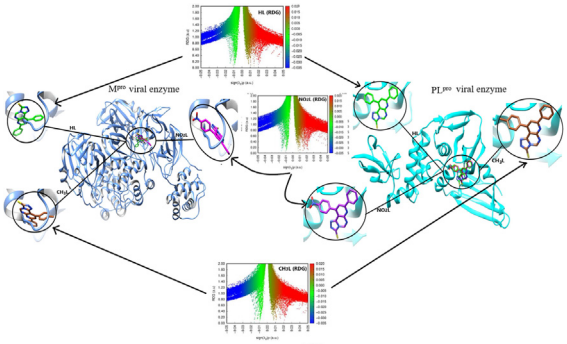

ARTICLE INFO

Article history:
Received 18 March 2021
Received in revised form 30 April 2021
Accepted 23 May 2021
Available online 26 May 2021

Keywords:
DFT study
Heterocyclic compounds
Spectroscopic analyses
Geometrical calculation
Non-covalent interaction
Molecular docking
SARS-Cov-2

ABSTRACT

Investigation the molecular structure of the system requires a detailed experience in dealing with theoretical computational guides to highlight its important role. Molecular structure of three heterocyclic compounds 8,10-diphenylpyrido[3,2–e][1,2,4]triazolo[4,3–c]pyrimidine-3(2H)-thione (**HL**), 8-phenyl-10-(p-tolyl)pyrido[3,2–e][1,2,4]triazolo[4,3–c]pyrimidine-3(2H)-thione (**CH_3L**) and10-(4-nitrophenyl)-8-phenylpyrido[3,2–e][1,2,4]triazolo[4,3–c]pyrimidine-3(2H)-thione (**NO_2L**) was studied at DFT/B3LYP/6-31G (d,p) level in ethanol solvent. Spectroscopic properties such Infrared (IR, ^{1}H NMR and ^{13}C NMR) and ultraviolet–visible (UV–VIS) analyses were computed. Some quantum and reactivity parameters (HOMO energy, LUMO energy, energy gap, ionization potential, electron affinity, chemical potential, global softness, lipophelicity) were studied, also molecular electrostatic potential (MEP) was performed to indicate the reactive nucleophilic and electrophilic sites. The effects of H-, CH_3– and NO_2– substituents on heterocyclic ligands were studied and it was found that the electron donation sites concerned with hydrogen and methyl substituents over nitro substituent. Topological analysis using reduced density gradient (RDG) was discussed in details. To predict the relevant antiviral activity of the reported heterocyclic compounds, molecular docking simulation was applied to the crystal structure of SARS-Cov-2 viral M^{pro} enzyme with 6WTT code and PL^{pro} with 7JRN code. The enzymatic viral protein gives an image about the binding affinity between the target protein receptor and the heterocyclic ligands entitled. The hydrogen bonding interactions were evaluated from molecular docking with different strength for each ligand compound to discuss the efficiency of heterocyclic ligands toward viral inhibition.

* Corresponding author.
E-mail address: doaa.saeed@alexu.edu.eg (D.S. El Sayed).

https://doi.org/10.1016/j.saa.2021.120006
1386-1425/

1. Introduction

2-amino-3-cyanopyridines are good starting reagents that have been used to synthesize many heterocyclic compounds such as pyridopyrimidines [1,2], [1,2,4]triazolo and [1,2,3,4] tetrazolo derivatives. Pyridopyrimidines are interesting compounds for its biological activities such as anti-microbial and cytotoxic activities [3]. At this time, studies have been intensified on the causes and forms of different types of cancers and how to find solutions to treat them or limit their occurrence. Ligands of low molecular weight, such as Schiff bases and heterocyclic compounds, can bind to protein receptors by forming a number of non-covalent interactions of different amino acid residues. Interactions between different non-covalent molecules are weak compared to covalent bonds because a variety of non-covalent interactions do not include electron sharing. Types of interactions between ligands and protein target include π–π aromatic stacking [4,5], hydrogen bonds [6,7] hydrophobic effects, [8,9], cation–π interactions, [10,11] halogen bonds, [12,13] and salt bridges [14,15]. π–π stacking is defined as a noncovalent attractive interaction between the aromatic rings, but this type not as widespread as hydrophobic contacts and hydrogen bonds, this type plays a major role in biological molecular recognition and the organization of structural biomolecules. The study of geometrical and energetic properties of these non-covalent interactions is mainly important in various applications of drug discovery [11,16,17]. Egli and his co-workers first reported that formation a non-covalent contact between the lone pair of O4′ atom of cytosine deoxyribose and the π cloud of the aromatic system of guanine nucleobase that stabilizes the structural component of the Z-DNA double-helix structure [18]. This type of interaction is called lone pair–π (lp–π) interaction. There are many organic heterocyclic ligands [19–21] that have been studied according to their applications in pharma, drug and catalysis. To relate heterocyclic ligands with their complexes, complexes with transition metals get a great attention due to extensive applications in fields such as antibacterial, antiviral and flame retardant [22,23]**.** Cancer treatment with coordination complexes was considered to be a great success since the discovery of cisplatin. [24].

This study aimed to elucidate the structural, electronic and molecular antiviral properties of **HL**, **CH_3L** and **NO_2L** heterocyclic ligand compounds with DFT computational study. These compounds have been experimentally synthesized with spectral characterization occurred [25]. Scheme 1 shows the structures of heterocyclic ligands afforded in this study. The binding modes of different substituents (H, CH3 and NO2) to the phenyl ring of the parent compound of the hydroxyl group were investigated with complete computational details.

Spectroscopic features such as electronic circular dichroism is termed as the differential absorption of left and right circularly polarized electromagnetic radiation by a sample, this analysis is also defined as chiroptical counterpart of UV–Vis absorption spectroscopy. Similarly, Raman spectroscopy is the counterpart of infrared (IR). The main advantages of chiroptical spectroscopic, instead of non-chiral identification, are sensitive to the absolute configuration of a sample. This type of chiroptical spectroscopies is sensitive toward the all molecular structure rather than their non-chiral counterpart. ECD spectrum involves a lot of structural information about the molecular structure such conformation and configuration [26]**.**

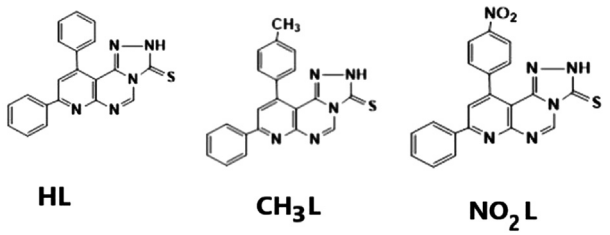

Scheme 1. The chemical structure of recently synthesized heterocyclic compounds [25].

2. Method of calculation

2.1. Experimental

The heterocyclic compound class was synthesized as the reported method presented by El-sayed *et al* [25] Infrared spectra were measured on Perkin-Elmer FT/IR spectrophotometer, ^{1}H NMR and ^{13}C NMR spectra were measured on (300 MHz), in solvent DMSO d_6, using the internal reference standard tetramethylsilane (TMS).

2.2. Computational details

Computational study has been performed to evaluate the structural properties of three heterocyclic compounds **HL**, **CH_3L**, **NO_2L**. Gaussian 09 software [27] was used for this calculation based on density functional theory (DFT). The selected computational method is using Becke's three parameter exchange function [28,29] from the Lee Yang Parr (B3LYP) correlation function with polarized basis set 6-31G (d,p). the calculations were performed in ethanol using the model of conductor-like polarizable contimum (CPCM) with no imaginary frequency [30]**.** Gauss view software [31] and Chemcraft program [32] were used to create the Gaussian input file and visualize the optimized structure. IR spectra and UV/visible properties of the optimized compounds were performed and calculated at the same level of DFT theory. ^{1}H and ^{13}C NMR spectral analyses were performed after optimization using the gauge-including-atomic-orbital (GIAO) method. UV–VIS study was followed by time-dependent density functional theory (TD-DFT) method [33] to confirm different electronic transitions in the heterocyclic ligands. Some quantum chemical parameters were estimated for the optimized structures to get an information about their stability and reactivity. Topological analysis was considered as it is helpful in the interaction findings between atoms at the structure surface. Molecular electrostatic potential (MEP) was applied to investigate the electrophilic and nucleophilic binding sites. Non covalent interaction analysis using reduced density gradient (NCI-RDG) were analyzed which is helpful in illustrating the type of intramolecular interactions.

2.3. Molecular docking simulation

The heterocyclic ligands, **HL**, **CH_3L**, **NO_2L**, are withdrawn to docking simulation with the crystal structure of M^{pro} and PL^{pro} targets with 6WTT and 7JRN codes were downloaded from Protein Data Bank (PDB) (https://www.rcsb.org/structure). iGemdock 2.1 software [34] was used for docking calculations and Chimera 1.13.1 [35] was used for ligand-target interaction visualization. The docking technique default setting is based on X-ray diffraction with resolution of 2.30 Å and R-factor of 0.193 with total residue count of 207. The docking accuracy settings (GA parameters) was adjusted as a standard docking of population size 200, generations 70 and number of solutions 2. The receptor was prepared by removing any ions, small ligands and water molecules and addition of polar hydrogens.

3. Results and discussion

3.1. Geometry optimization

The optimized heterocyclic structures related to ground state were obtained in ethanol at B3LYPl6-31G(d,p) are shown in Fig. 1 with labeling atoms geometrical parameters data (bond length, bond angle and some dihedral values). Most of geometrical parameters are similar for the structure derivatives, while the difference appears in the geometry of the substituent on the phenyl ring branched from C2 atom. The dihedral value of S-C-N-H differs for **CH_3L** (-0.13) that may be attributed to the methyl group on the phenyl ring make it appear far from the triazole ring, where the geometry of triazole moiety became more planar than the other of the two heterocyclic ligands. The optimized structures show a close contact between the phenyl group carry the substituent and the triazole ring, that slightly changes the plane position of triazole ring and the dihedral values also change (for **HL** is −0.23 and for **NO_2L** is −0.24). Table 1 shows Mulliken charges calculated on each atom where most of charges in the three ligands are the same except the charges of newly added substituent atoms in each ligand which makes the surrounded electronic environment differ from one ligand to another. In the three derived ligands, N5 and N11 have approximately similar high charges (-0.536 and −0.563), but the charge on N14 (-0.350) and N15 (-0.383) have small charges. In the case of Sulphur, It has a small charge (-0.258 for **HL**, −0.260 for **CH_3L** and −0.245 for **NO_2L**) compared with other nitrogen atoms.

3.2. IR spectral analysis

Vibrational spectra of the studied ligands were calculated to ensure their molecular structures. There are some characteristic bands for the three ligands shown in Fig. 2**.** There is a sharp band appeared at 3679 cm^{-1}, 3651 cm^{-1} and 3679 cm^{-1} for **HL**, **CH_3L** and **NO_2L**, respectively that attributed to N-H of triazole ring stretching. The experimental data revealed that presence of a band at 3377 cm^{-1}, 3356 cm^{-1} and 3332 cm^{-1} which were corresponding to NH group of **HL**, **CH_3L** and **NO_2L**, respectively. The difference in theoretical and experimental data matching can be attributed to the solvent environment in the preparation method, also computational study performed calculations in pure ethanol, but not in

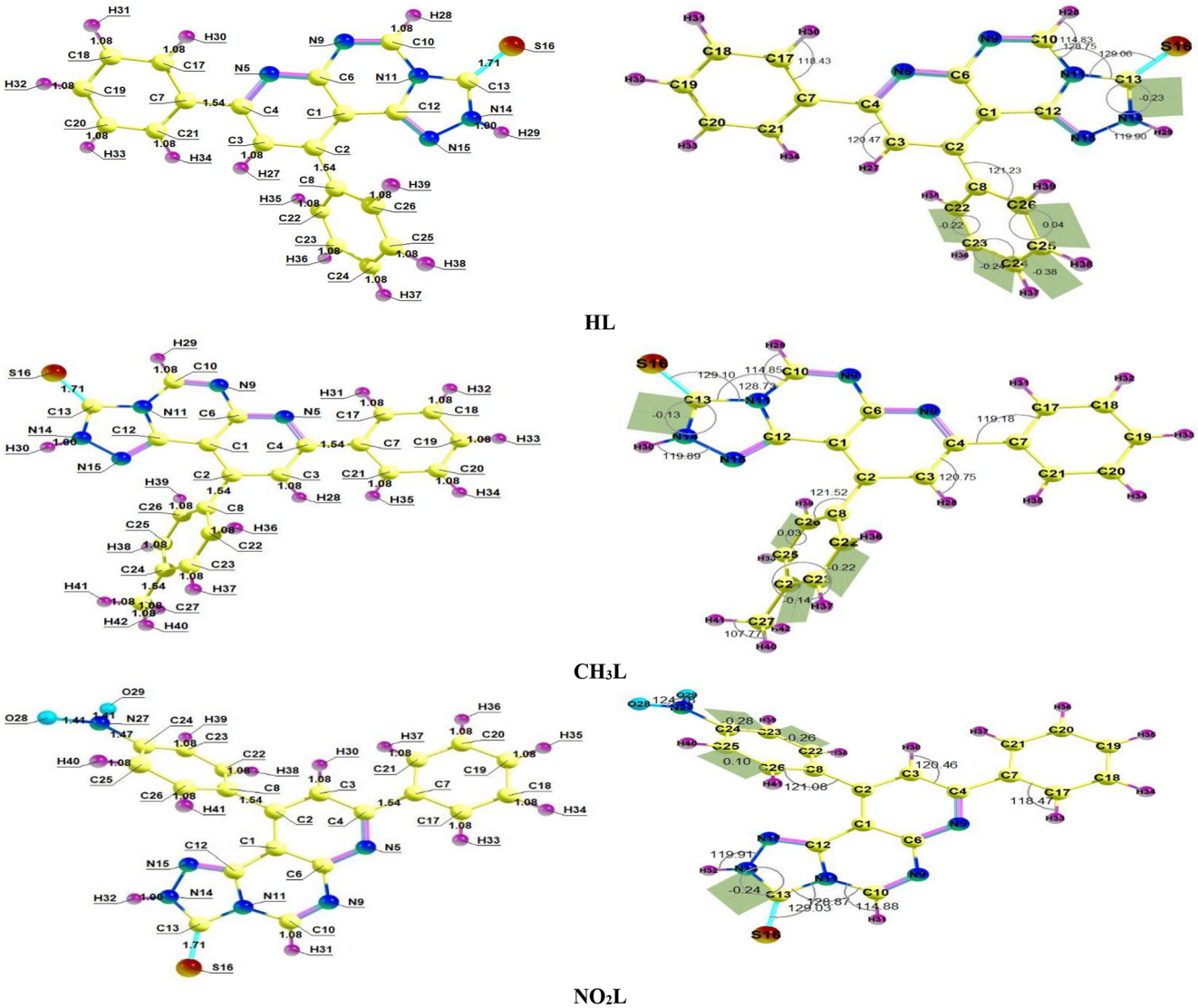

Fig. 1. Labelled optimized heterocyclic compounds with bond lengths, some bond angles and dihedral values.

Table 1
Mullikan atomic charge distribution of **HL**, **CH_3L** and **NO_2L** heterocyclic compounds.

HL		CH_3L		NO_2L	
C1	0.096	C1	0.096	C1	0.101
C2	0.032	C2	0.035	C2	0.026
C3	−0.141	C3	−0.138	C3	−0.138
C4	0.265	C4	0.274	C4	0.267
N5	−0.536	N5	−0.544	N5	−0.533
C6	0.355	C6	0.355	C6	0.358
C7	0.068	C7	0.065	C7	0.068
C8	0.043	C8	0.040	C8	0.059
N9	−0.462	N9	−0.462	N9	−0.461
C10	0.320	C10	0.320	C10	0.322
N11	−0.563	N11	−0.564	N11	−0.564
C12	0.531	C12	0.531	C12	0.534
C13	0.354	C13	0.354	C13	0.353
N14	−0.350	N14	−0.349	N14	−0.350
N15	−0.383	N15	−0.384	N15	−0.389
S16	−0.258	S16	−0.260	S16	−0.245
C17	−0.096	C17	−0.097	C17	−0.095
C18	−0.092	C18	−0.092	C18	−0.092
C19	−0.076	C19	−0.075	C19	−0.074
C20	−0.096	C20	−0.097	C20	−0.096
C21	−0.118	C21	−0.120	C21	−0.118
C22	−0.101	C22	−0.101	C22	−0.114
C23	−0.089	C23	−0.128	C23	−0.092
C24	−0.078	C24	0.131	C24	0.251
C25	−0.092	C25	−0.125	C25	−0.094
C26	−0.065	C26	−0.064	C26	−0.077
H27	0.108	C27	−0.383	N27	0.387
H28	0.171	H28	0.105	O28	−0.393
H29	0.307	H29	0.171	O29	−0.394
H30	0.124	H30	0.306	H30	0.111
H31	0.094	H31	0.127	H31	0.174
H32	0.091	H32	0.093	H32	0.310
H33	0.090	H33	0.091	H33	0.126
H34	0.084	H34	0.090	H34	0.097
H35	0.092	H35	0.084	H35	0.094
H36	0.092	H36	0.092	H36	0.093
H37	0.092	H37	0.084	H37	0.084
H38	0.092	H38	0.083	H38	0.110
H39	0.093	H39	0.092	H39	0.143
–	–	H40	0.113	H40	0.142
–	–	H41	0.127	H41	0.110
–	–	H42	0.126	–	–

solid state. Another band appears at 3205 cm^{-1} for **HL**, 3169 cm^{-1} **CH_3L** and 3201 cm^{-1} **NO_2L** that attributed to C-H aromatic stretching, respectively [36]. There is a strong and sharp band at 1631 cm^{-1} for **HL**, 1593 cm^{-1} for **CH_3L** and 1620 cm-1 for **NO_2L** where these data corresponding to C = N group positions that experimentally appears at the same positions (1624 cm^{-1} for HL, 1617 cm^{-1} for **CH_3L** and 1605 cm^{-1} for **NO_2L**).

Bands at 1520 cm^{-1} and 1263 cm^{-1} are corresponding to C = C and C = S groups of **HL**, respectively. Bands appearance at 1510 cm^{-1} and 1253 cm^{-1} are corresponding to C = C and C = S groups of **CH_3L**, respectively. Bands appearance at 1524 cm^{-1} and 1263 cm^{-1} are corresponding to C = C and C = S groups of **NO_2L**, respectively. Backing to the experimental results, it was found two bands 1596 cm^{-1}, 1589 cm^{-1}, 1574 cm^{-1}which were corresponded to C = C group of **HL**, **CH_3L** and **NO_2L**, respectively. where the results are slightly closer to the experimental result. Experimental IR C = S band appears at 1274 cm^{-1}, 1263 cm^{-1} and 1282 cm^{-1} that give similar calculated results. Also, there is a strong and sharp band at 1267 cm^{-1} which is corresponding to N-H bending mode in the case of **CH_3L**, a small band is appeared at 2925 cm^{-1} which is corresponding to C-H of alkyl stretching. In case of **NO_2L**, there are two sharp stretching bands at 1669 cm^{-1} and 1383 cm^{-1} due to presence of NO_2 group where one of its band is interfered with the position of C = N group of aromatic ring.

3.3. ^1H and ^{13}C NMR spectral investigation

To make a comparison between experimental and theoretical NMR spectral analysis, GIAO method was applied of the B3LYP/6-31G (d,p) optimized compounds. Fig. 3 shows ^1H and ^{13}C NMR spectral analysis of the three studied heterocyclic compounds. In case of ^1H NMR of **HL**, position of Ar-H peak at δ = 7.41 ppm – 8.33 ppm, the range is similar to the experimental values of δ 7.13–8.17 (m, 10*H*, Ar-H). but the chemical shift of N-H appears at 13.83 ppm where experimentally differs which is 8.49 ppm (s, 1H, NH, D_2O exchangeable); that may be due to the experimental interaction mode of the proton with other surrounded atoms. The peak of H-pyridinic proton appears at 8.10 PPM and experimentally occurs at 8.25 (s, $H\text{-}_5$ pyridinic proton). For Ar-H of pyrimidine, it located at 8.63 ppm and that coincides with the experimental result which showed 8.34 (s, 1H, Ar-H of pyrimidine). In case of ^{13}C NMR of **HL**, C_3 of pyridine ring locates at 119.7 ppm and experimentally occurred at 129.3. C_4 of pyridine ring locates at 148.5 ppm and experimentally occurred at 149.35 ppm. C_2 of pyridine ring present at 157.7 ppm and experimentally present at 155.9 ppm. The peak of C = S appears at 139.8 ppm which differ from the experimental value (182.47 ppm). In case of **CH_3L**, ^1H NMR of CH3 group protons present at 2.34 ppm, while experimentally present at 2.83 ppm (s, 3H, CH_3). Aryl protons location range from 7.15 ppm to 8.33 ppm, experimentally the range is 6.96 ppm −8.13 ppm (m, 9H, Ar-H). $H\text{-}_5$ pyridinic proton shifts 8.63 ppm while it experimentally appears as strong peak at 8.31 ppm. Ar-H of pyrimidine present at 8.10 ppm while experimentally at 8.42 ppm.

In case of **NO_2L,** ^1H NMR Ar-H peaks range from 7.49 ppm to 8.33 ppm and experimentally a medium peaks appeared in the range from 7.11 ppm −8.28 ppm. NMR peak of $H\text{-}_5$ pyridinic proton locates at 8.63 ppm, experimentally a strong peak is shifted at 8.33 ppm. Ar-H of pyrimidine peak appears at 8.10 ppm, while experimentally was found at higher chemical shift 8.48 ppm. Concluding these results, there is a good matching between experimental and theoretical characterization in the most cases.

3.4. UV–Vis electronic spectra using TD-DFT method

Describing the electronic behavior of **HL**, **CH_3L** and **NO_2L**, TD-DFT was applied with CPCM as solvation model. Gaussian 09 default settings were applied for TD-DFT calculations. The program settings were adjusted for Nstate = 6 for analysis of six states. It was shown from Fig. 4 that there are three transition bands present as lines for **HL**, **CH_3L** and **NO_2L**. From the LOG file of Gaussian calculation, the first transition represents a singlet strong absorption band with orbital contribution of HOMO-LUMO and HOMO-LUMO + 1 for **HL** and **CH_3L** but only HOMO-LUMO orbital contribution was present for **NO_2L** that corresponding to n-π^* transition. LOG outputs estimated the probability of presence this transition as a % with energy of 3.318 eV, 3.317 eV and 2.842 eV at λ_{max} 373.7 nm, 373.8 nm and 436.3 nm for **HL**, **CH_3L** and **NO_2L**, respectively. Also, the second singlet line represents electronic transition from HOMO-LUMO and HOMO-LUMO + 1 that corresponding to n-π^* transition for **HL** and **CH_3L**.

(Fig. 4 **a,b**), while for **NO_2L**, the contribution appeared in HOMO → LUMO + 1 and HOMO → LUMO + 2 with quite smaller energy value (3.354 eV) and higher λ_{max} (369.7 nm). Furthermore, the bands shape of **HL** and **CH_3L** heterocyclic ligands are quite similar, while in case of **NO_2L**, the band shape and lines position differ as shown in Fig. 4**c**. To summarize these calculations, closing the band shape and wavelength values indicate the identical electronic structure of **HL** and **CH_3L**, but **NO_2L** was attributed as a different electronic behavior system. Fig. 5 it was found that in the third excitation level, the orbital contribution of **NO_2L** electronic structure

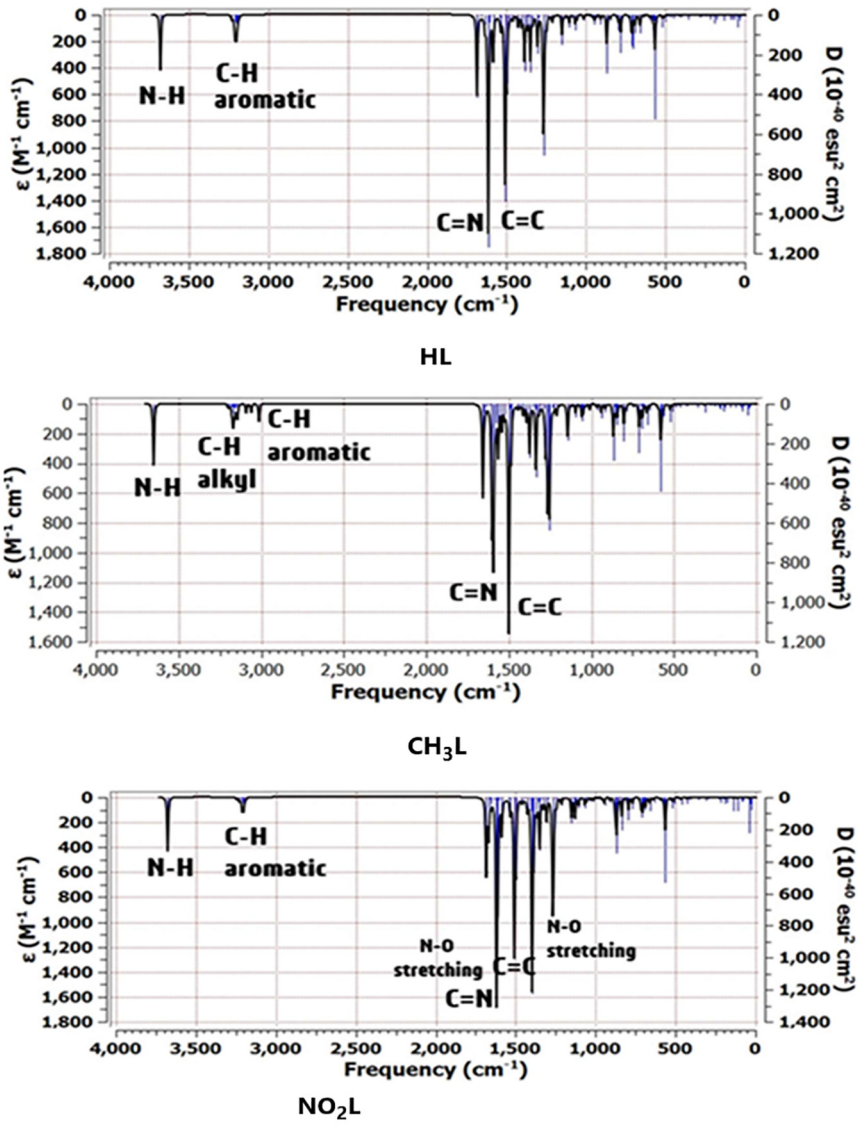

Fig. 2. Calculated IR spectra of heterocyclic compounds at B3LYP/6-31G(d,p) level.

differ from the other ligands. The orbital contribution character can be estimated from the counter diagrams present for **HL**, **CH_3L** and **NO_2L**. LUMO + 2 orbital of **NO_2L** compound contributed on nitro group but in the other two heterocyclic compounds, the substituents mostly appear no contribution character. Table 2 shows excitation energies, maximum wavelengths, oscillator strengths and % orbital contribution for **HL**, **CH_3L** and **NO_2L** compounds.

Also, Fig. 4 illustrates the different features of ECD plot for each studied ligand. Similar ECD peaks are obtained for **HL** and **CH_3L** but the peak of **NO_2L** differently occur. In case of **HL** and **CH_3L**, the first singlet peak, appeared as (-) camphor, while the other two singlet peaks appeared as a (+) camphor. This indicated that the two ligands are identical in UV–Vis spectra and also in conformation and configuration of atoms in the molecular system. In case of the **NO_2L**, all the singlet peaks appeared in a (+) camphor, that confirmed the completely different configuration structure with respect to the other two heterocyclic ligands.

3.5. Molecular orbital energies and reactivity

The energies of molecular orbitals HOMO and LUMO were evaluated for the three tested optimized ligands in gas phase to calculate the energy gap of these ligands. The results can give an indication about the reactivity of molecules associated with chemical reactions [37]**.** The most of orbital contribution on HOMO for the three ligands include triazole ring with sulfur atom, but the orbital contribution on LUMO for **HL** and **CH_3L** include the pyrimidine ring with one substituted phenyl group but for **NO_2L**, most of orbital contribution is attributed to nitro-phenyl group. Energy gap of **HL** (E_{GAP} = 3.642 eV) and of **CH_3L** (E_{GAP} = 3.635 eV) appear to be closer in values, so, their reactivity is the same but energy gap of **NO_2L** (E_{GAP} = 3.183 eV) is slightly with smaller value, so it is reactive towards an electrophile through a nucleophilic part occurred in the molecule. Fig. 6 shows a description of molecular orbitals with transition for the three ligands with energy values of HOMO, LUMO and HOMO/LUMO energy gap. Table 3 shows some important calculated reactivity parameters elucidated from the optimized structures that can explain the electronic behavior of the titled compounds. Such parameters are, total energy of the molecule, ionization potential, electron affinity, chemical potential, chemical hardness, softness and energy fraction. The studied parameters such dipole moment, chemical hardness and energy fraction are with lower values in case of **NO_2L** compared with other ligands. Other parameters such ionization potential, electron

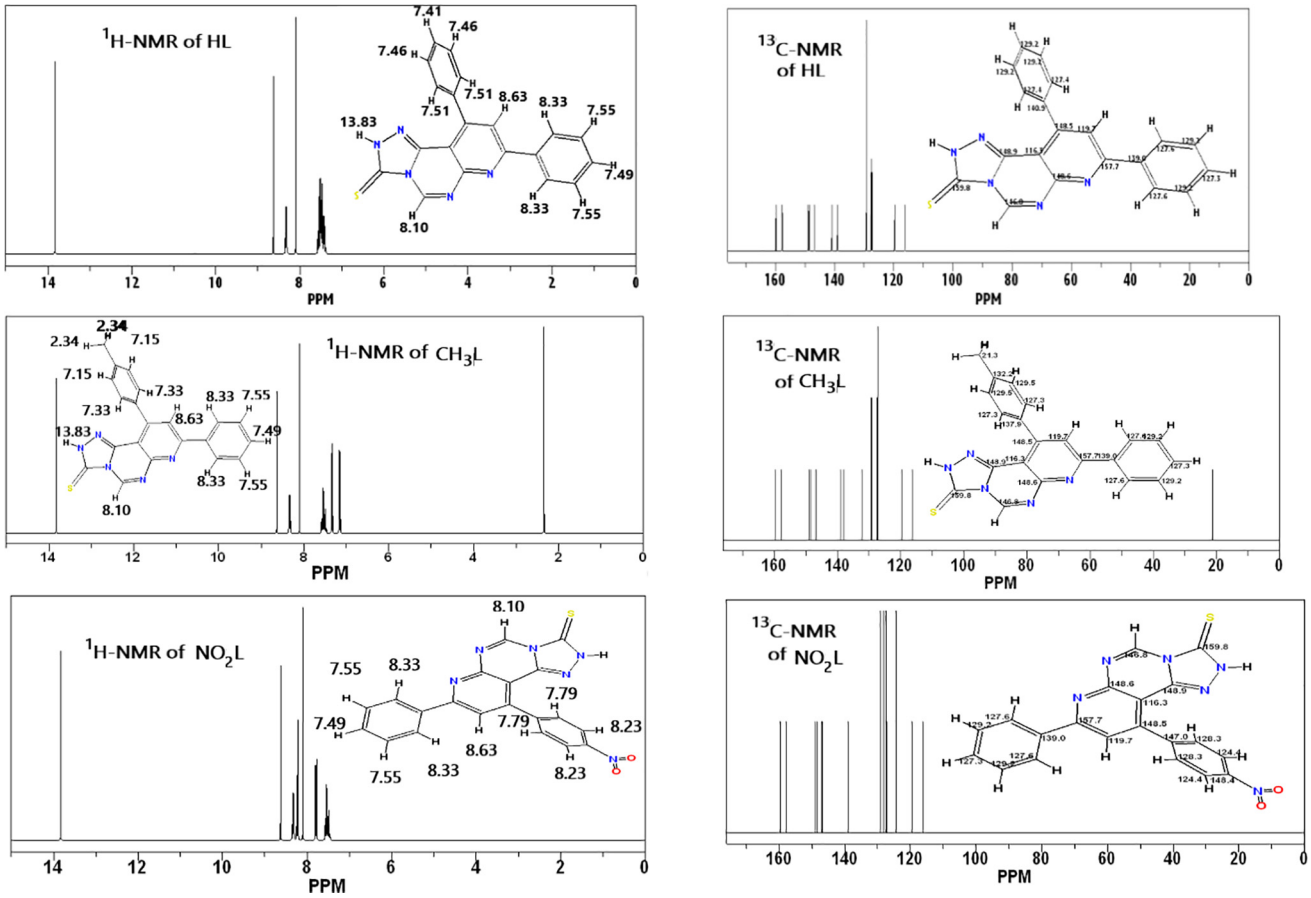

Fig. 3. ^{1}H NMR and ^{13}C NMR spectra of HL, CH_3L and NO_2L using GIAO method on the optimized heterocyclic structures.

affinity, chemical potential and softness are higher values in case of **NO_2L** compared with the other ligands. We can say from this part that **NO_2L** acts as a nucleophile through nitro group slightly stronger than the other ligands.

3.6. Topological surface study

3.6.1. Molecular electrostatic potential (MEP) analysis

Reactivity of the heterocyclic compounds was deduced by analysis of the molecular electrostatic potential (MEP) surface. Detecting the inter and intramolecular interactions in the studied compounds was confirmed by elucidation the electron-rich and electron-poor molecular sited. As shown from Fig. 7, the electron-rich sites are attributed to one phenyl group carried on pyridine ring and also nitrogen atom of pyridine, this represented as an orange-yellow color on the surface of **HL**, **CH_3L** and **NO_2L** ligands. Electron-poor sites are attributed to the triazole ring which represented with blue color on the surface of the ligands. For further illustration, the triazole ring is termed as a nucleophilic center and nitrogen of pyridine ring is termed as an electrophilic center. Furthermore, methyl group substituent of **CH_3L** ligand appeared with blue code color, so it is positively charged center and the nitro group substituent of **NO_2L** ligand is colored with yellow code color, that means it is a weekly negatively charged center.

3.6.2. Non covalent interaction analysis (NCI-RDG analysis)

Investigating NCI bonds in the molecular atoms predict, in the future, the behavior of atomic sites for interaction towards other molecular atoms. Reduced density gradient analysis is determined in function of sign sign(λ2)ρ parameter which describes the multiplication of the electron density with the sign of the second Hessian eigenvalue. Diagrams extracted from this analysis are represented in colored codes [38,39]**.** As shown from Fig. 8, **HL**, **CH_3L** and **NO_2L** ligands were manipulated as plots with a number of weak and strong spikes. To illustrate the type of interactions, it should be understanding the code colors where blue color refers to hydrogen bond formation, green color refers to Van der Waals attraction and red color refers to steric repulsion interaction. In all ligands, there is Van der Waals interaction in between the substituted phenyl ring and triazolo moiety. Also, Van der Waals occur between sulfur atom and pyrimidine ring. Steric repulsion interaction is present inside the aromatic rings for all compounds. There is a slight difference in interaction sites due to exchangeable substituent. In case of **CH_3L**, there is a weak repulsion interaction between the tolyl ring and pyridine ring that may be attributed to the bulkiness of the whole tolyl moiety around the remaining molecular part. In case of **NO_2L**, there is a strong repulsion interaction between nitro group and its phenyl carrier, this feature is not appeared in **HL** and **CH_3L** ligands, that may be due to the bulkiness of nitro group that take a certain geometry on the structure. From the colored RDG plot of all ligands, spike with negative sign(λ2)ρ sign represents Van der Waals attraction between atoms of each ligand ($-0.02 < \text{sign}(\lambda_2)\rho < 0$). Spike represents highly negative sign(λ_2)ρ value ($-0.02 > \text{sign}(\lambda_2)\rho$) attributed to hydrogen bond formation and this feature not present in the studied ligand structure due to the small electron density on the surface leading to inability of hydrogen bond formation. The spike with positive value (sign (λ_2) $\geq$ 0.01) represents strong steric repulsion between atoms of the molecule.

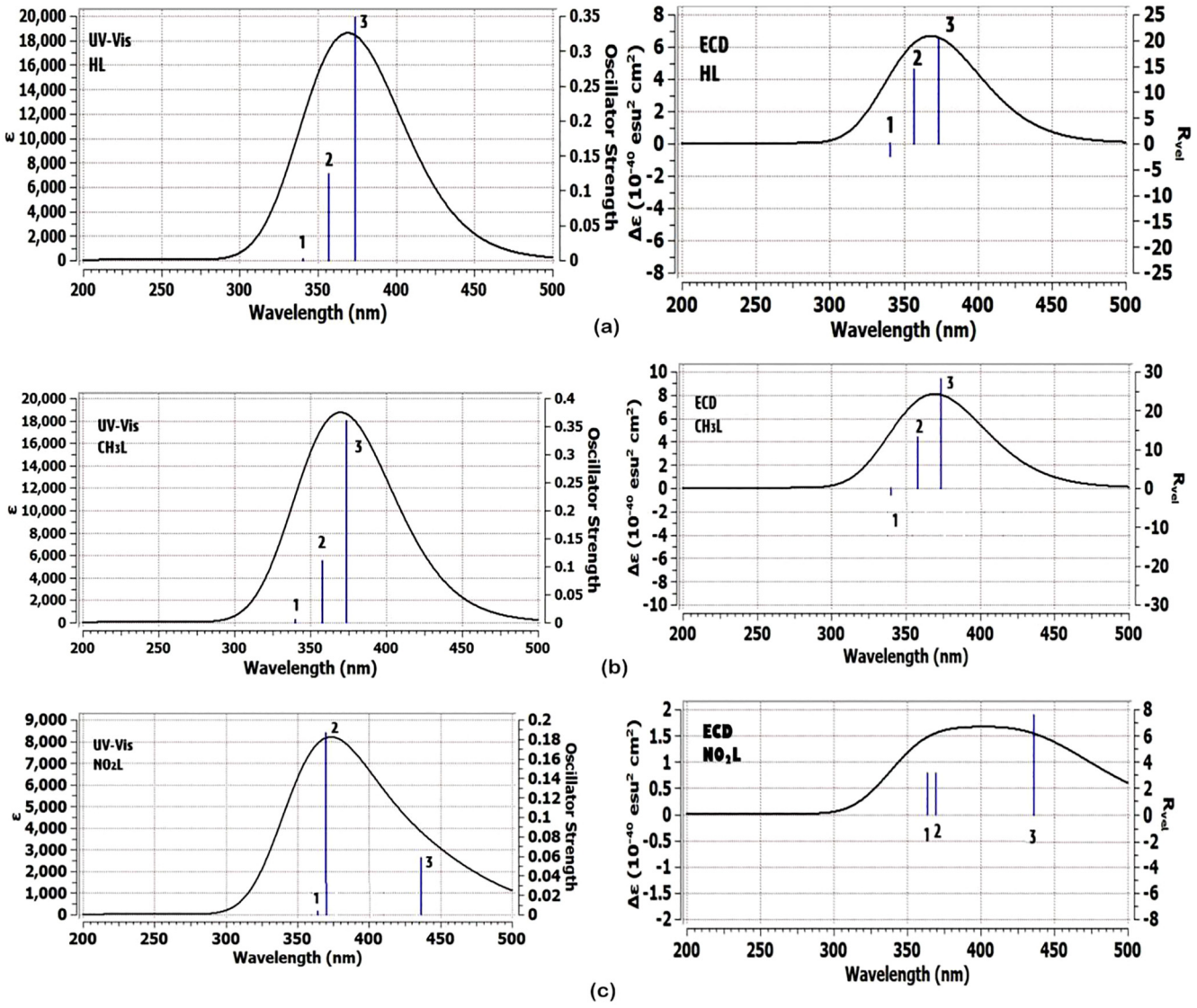

Fig. 4. UV–Vis and ECD electronic absorption spectra for (a) **HL**, (b) **CH_3L** and (c) **NO_2L** heterocyclic ligands.

3.7. Investigation of a potent antiviral activity

The optimized pyrimidine triazolo compound derivatives were docked in the active sites of M^{pro} enzyme applying 6WTT target and PL^{pro} enzyme using 7JRN target, as a docking receptor. Fig. 9 shows the strength of interactions of the three tested ligands with different amino acids that surround the docked ligands in M^{pro} enzyme. Fig. 11 shows the strength of interactions of the three tested ligands with different amino acids that surround the docked ligands in PL^{pro} enzyme.

3.7.1. Molecular docking study of triazole derivatives with M^{pro} of SARS-CoV-2

In-silico docking of three ligands with 6WTT investigate that there are two types of interactions, H-bond and VDW, where **HL** interact with 6 amino acids, while **CH_3L** interact with 5 amino acids and **NO_2L** interact with 8 amino acids. This investigation reflects that the docked ligand compounds have binding poses ensures a favorable binding modes with M^{pro} target of PDB 6WTT [39,40]. Fig. 10 shows the types of amino acids interacted with the tested ligands. The results of optimized **HL** docking reveals that there are 6 interacting amino acids in chain A of M^{pro} represented in GLU-166.A, ARG-188.A, THR-190.A, HIS-41, HIS-164 and GLN-189 with docking energy −113.5 kcal/mol. When the optimized **CH_3L** was docked into the target, 5 amino acids were found that interacted with the ligand which are represented in HIS-164.A, GLU-166.A, HIS-41.A , ARG-188.A and GLN-189.A with total docking energy −105.2 kcal/mol. When the optimized **NO_2L** was docked in the protein target, 8 amino acids are interacted with the ligand which are represented in GLY-143.A, SER-144.A, CYS-145.A, HIS-164.A and GLU-166.A, HIS-41.A, LEU-167.A and GLN-189.A with total docked energy −128.6 kcal/mol. Table 4 shows the names of interacted protein residues, bond length and bond energy of the active sites for each ligand. It was found that the **NO_2L** inhibit 4 amino acid active sites with H-bond formation and block other 4 amino acids by VDW interactions but the other studied ligands block from 2 to 3 amino acids by H-bond formation and 3 other active sites by VDW interactions. The higher inhibition power of **NO_2L** is mainly due to presence of nitro group which strongly interacted with GLY-143.A (-3.500 kcal/mol), SER-144.A (-7.995 kcal/mol) and CYS-145.A (-9.500 kcal/mol and −6.210 kcal/-mol) with 4H-bond. The three ligand compounds are common interacted with amino acids HIS-41.A and GLN-189.A by VDW interactions. Fig. 10 also shows H-bond and VDW interactions

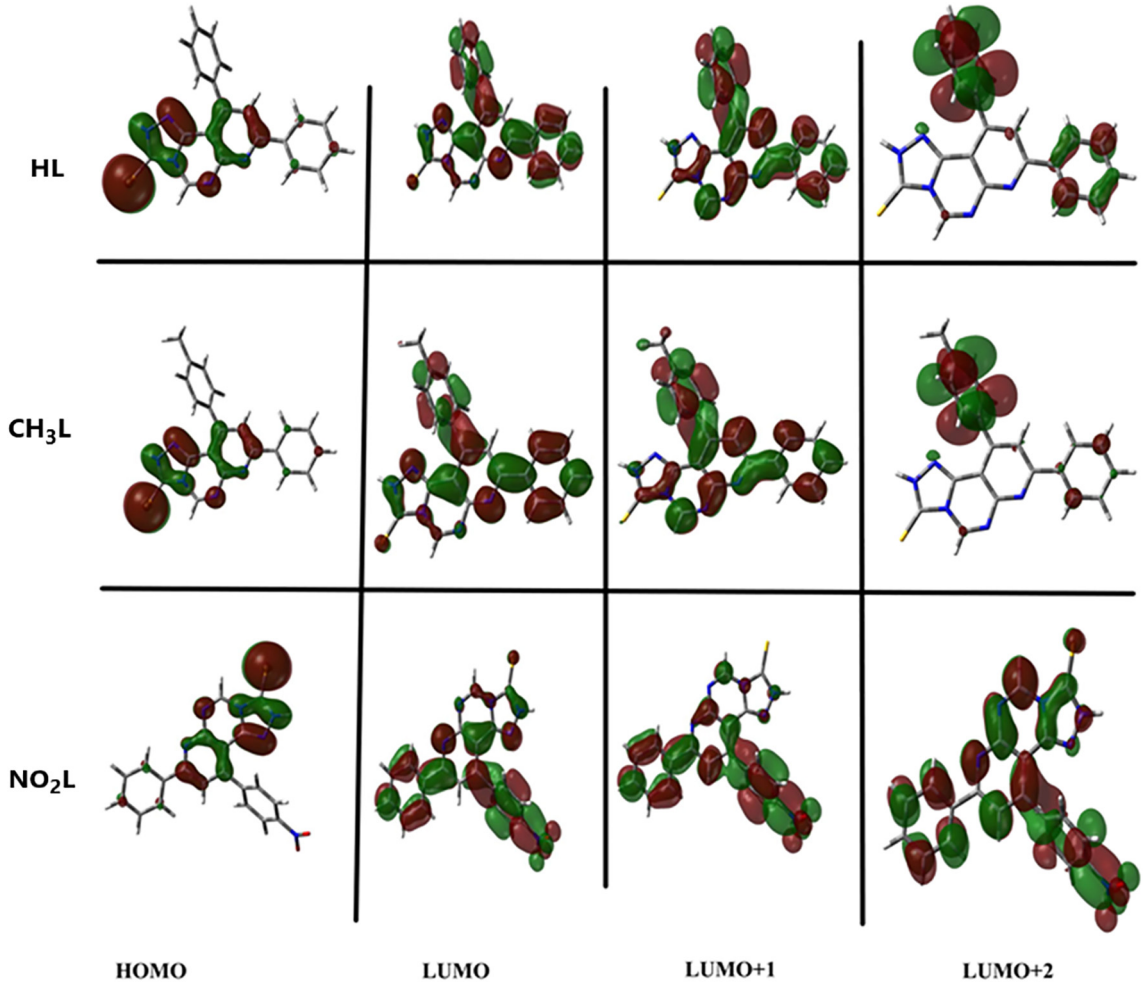

Fig. 5. Electronic singlet transition states molecular orbitals of **HL**, **CH_3L** and **NO_2L.**

Table 2
Excitation energies, maximum wavelengths, oscillator strengths and % orbital contribution for **HL**, **CH_3L** and **NO_2L** compounds.

Compound	Spectral line number	Excitation energy (eV)	λ_{max} (nm)	F	Type of transition	% orbital contribution
HL	1	3.318	373.7	0.3473	HOMO → LUMO	57.54
					HOMO → LUMO + 1	40.03
	2	3.473	357.0	0.1235	HOMO → LUMO	40.00
					HOMO → LUMO + 1	57.08
	3	3.640	340.6	0.002	HOMO-1 → LUMO	39.49
					HOMO-1 → LUMO + 1	55.83
CH_3L	1	3.317	373.8	0.3600	HOMO → LUMO	56.59
					HOMO → LUMO + 1	41.26
	2	3.464	357.9	0.200	HOMO → LUMO	41.13
					HOMO → LUMO + 1	56.08
	3	3.646	340.1	0.0050	HOMO-1 → LUMO	0.3548
					HOMO-1 → LUMO + 1	51.10
NO_2L	1	2.842	436.3	0.0580	HOMO → LUMO	70.43
	2	3.3537	369.7	0.1870	HOMO → LUMO + 1	36.18
					HOMO → LUMO + 2	59.71
	3	3.408	363.9	0.0030	HOMO-1 → LUMO	68.71
					HOMO-1 → LUMO + 1	13.34

between the surrounded amino acids of M^{pro} receptor and the tested ligands where the stick grey amino acids represent that interacted with H-bond formation and wire pink amino acids interact with ligands through VDW forces. We can investigate from this virtual screening that the nitro group substituent (polar group) of **NO_2L** is directed to be embedded inside the protein receptor, but the other 2 ligand substituents (non-polar H and CH3 groups) directed outside the protein receptor. This may be an evidence on the polar groups mostly like to be strongly docked within the protein receptor through formation of strong H-bond.

3.7.2. Molecular docking study of triazole derivatives with PL^{pro} of SARS-CoV-2

In-silico docking of three ligands with 7JRN investigate that there are two types of interactions, H-bond and VDW, where **HL** interact with 5 amino acids, while **CH_3L** interacts with 6 amino

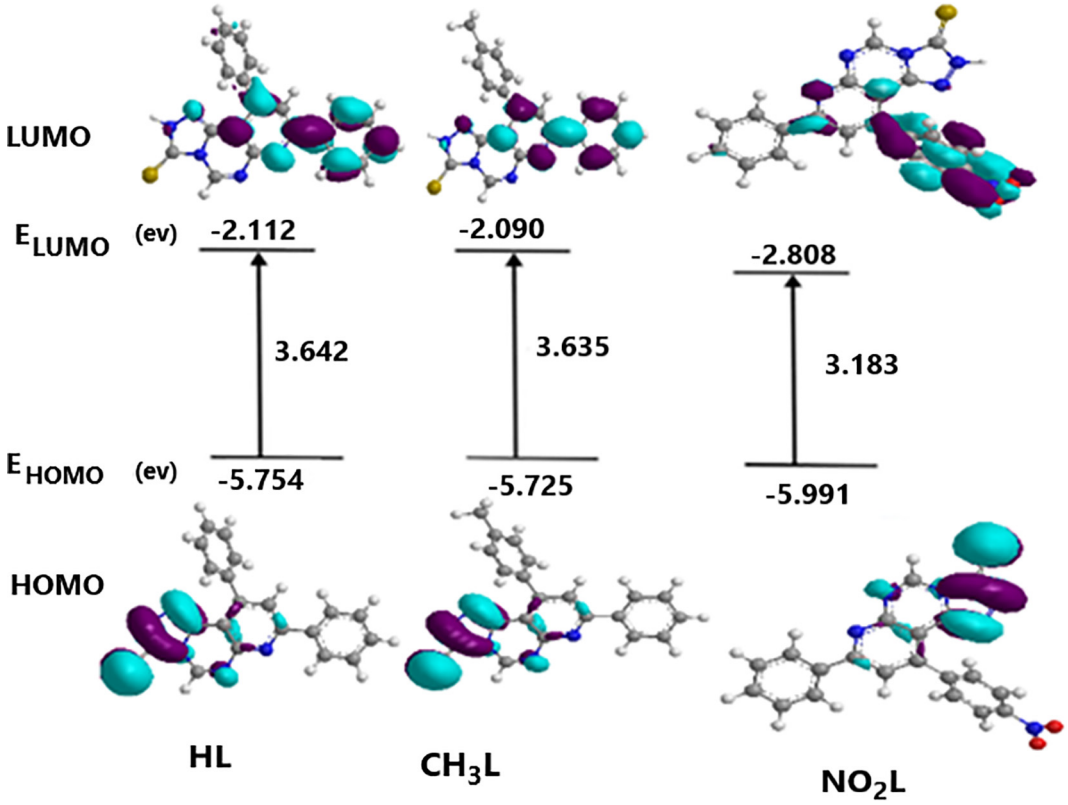

Fig. 6. Description of the molecular orbitals with calculated electronic transition for **HL**, **CH_3L** and **NO_2L.**

Table 3
Quantum chemical parameters of the studied compounds in gas phase.

Parameter	HL	CH_3L	NO_2L
Total energy (ev)	−39237.20	−40307.16	−44801.94
Dipole moment (Debye)	5.962	6.327	4.565
E_{HOMO} (eV)	−5.754	−5.725	−5.991
E_{LUMO} (eV)	−2.112	−2.090	−2.808
E_{GAP} (eV)	3.642	3.635	3.183
Ionization potential (eV)	5.754	5.725	5.991
Electron affinity (eV)	2.112	2.09	2.808
Chemical potential (eV)	3.933	3.908	4.399
Chemical hardness (eV)	1.821	1.818	1.592
Softness (eV)	0.549	0.550	0.628
Energy fraction (unitless)	2.724	2.739	2.133

acids and **NO_2L** interact with 8 amino acids. This investigation reflects that the docked ligand compounds have binding poses ensures a favorable binding mode with PL^{pro} target of PDB 7JRN.

Fig. 11 shows the types of amino acids interacted with the tested ligands. The results of optimized **HL** docking reveals that there are 5 interacting amino acids in chain A of PL^{pro} represented in ASP-164.A, ARG-166.A, TYR-264.A, TYR-268.A and GLN-269.A with docking energy −100.3 kcal/mol. When the optimized **CH_3L** was docked into the target, 6 amino acids can interact with the ligand which are represented in ASP-164.A, ARG-166.A, TYR-264.A, TYR-268.A, ASN-267.A and GLN-269.A with total docking energy −102.8 kcal/mol. When the optimized **NO_2L** was docked in the protein target, 8 amino acids can interact with the ligand which are represented in GLY-163.A, ASP-164.A, ARG-166.A, TYR-264.A ASN-267.A, TYR-268.A, GLN-269.A and TYR-273.A with total docked energy −107.6 kcal/mol. Table 5 shows the names of interacted protein residues, bond length and bond energy of the active sites for each ligand. We can investigate that **NO_2L** inhibit 3 amino acid active sites with H-bond formation and block other 6 amino acids by VDW interactions but the other studied ligands

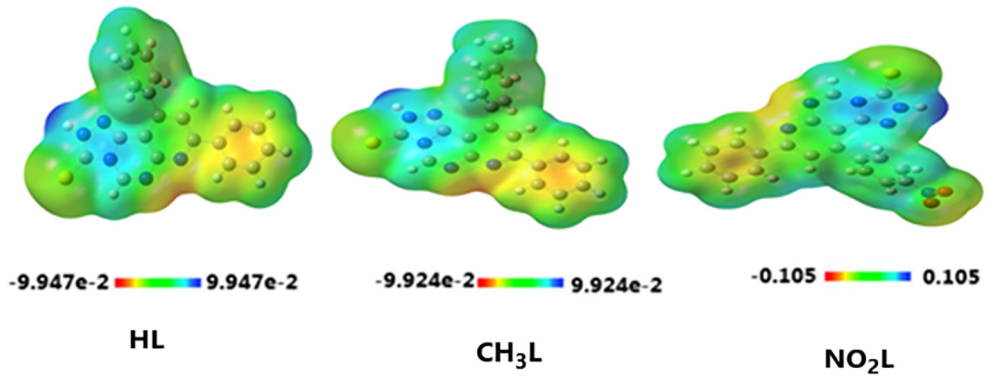

Fig. 7. MEP surface of the optimized structures of the heterocyclic ligands **HL**, **CH_3L** and **NO_2L.**

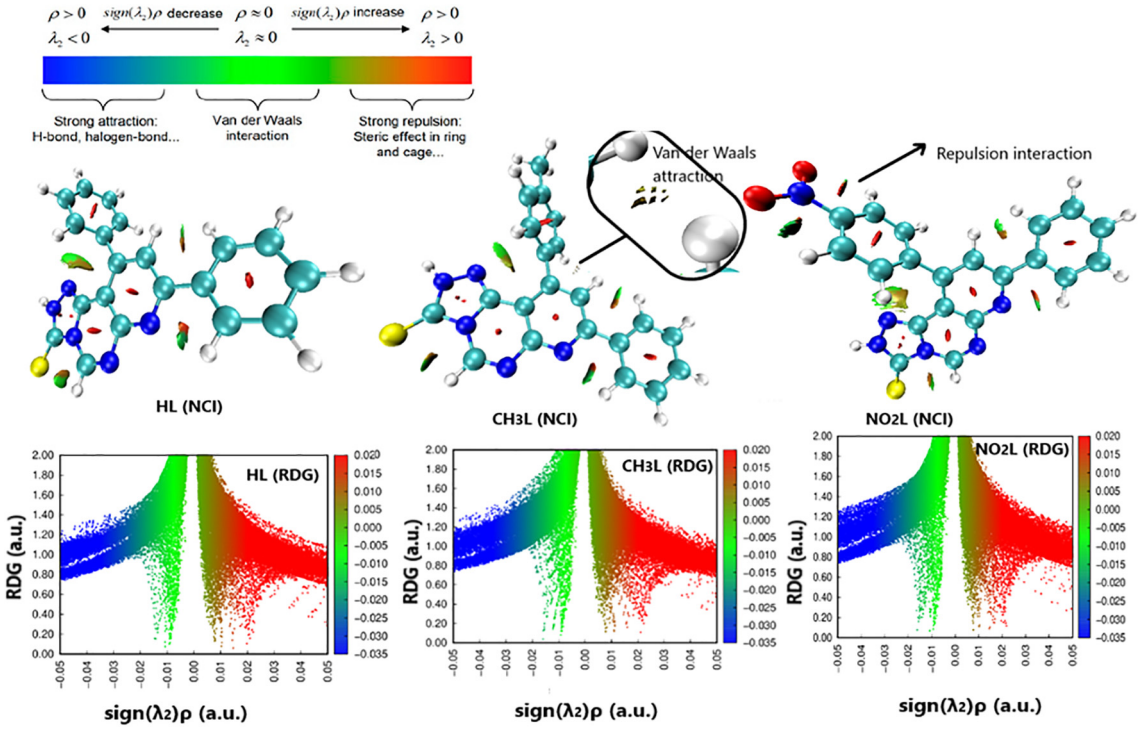

Fig. 8. NCI isosurfaces and RDG scatter mapping diagram of the optimized structures of **HL**, **CH_3L** and **NO_2L** heterocyclic compounds.

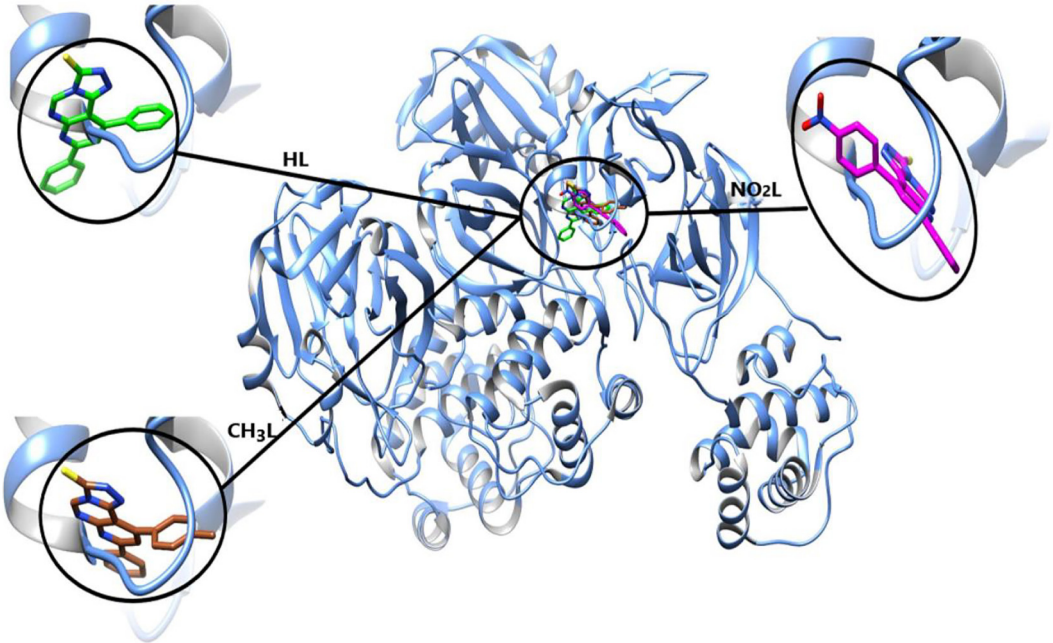

Fig. 9. Molecular docking of the studied heterocyclic ligands, **HL**, **CH_3L** and **NO_2L** with M^{pro} enzyme (PDB :6WTT).

block from 2 amino acids by H-bond formation and 3 other active sites by VDW interactions. The higher inhibition power of **NO_2L** is mainly due to presence of nitro group which strongly interacted with GLY-163.A (-3.467 kcal/mol), ASP-164.A −7.718 kcal/mol) and ARG-166.A (-6.533 kcal/mol) with 3H-bond. There are 3 common amino acids interacted with the three ligands (TYR-264.A, TYR-268.A and GLN-269.A) with a strong VDW interaction. Fig. 12 shows H-bond and VDW interactions between the surrounded amino acids of PL^{pro} receptor and the tested ligands where the stick grey amino acids represent that interacted with H-bond formation and wire pink amino acids interact with ligands through VDW forces. We can investigate from this virtual screening that the three ligand substituents are directed in the same direction inside the protein receptor with different mode of interaction. Comparing the total binding energy results of the two proteases enzyme docking, we conclude that M^{pro} is more effective towards inhibition by triazolo pyrimidine derivatives than PL^{pro} protease. While triazolo compound derivatives give stronger VDW amino acid interactions with receptor in case of PL^{pro} relative to M^{pro}.

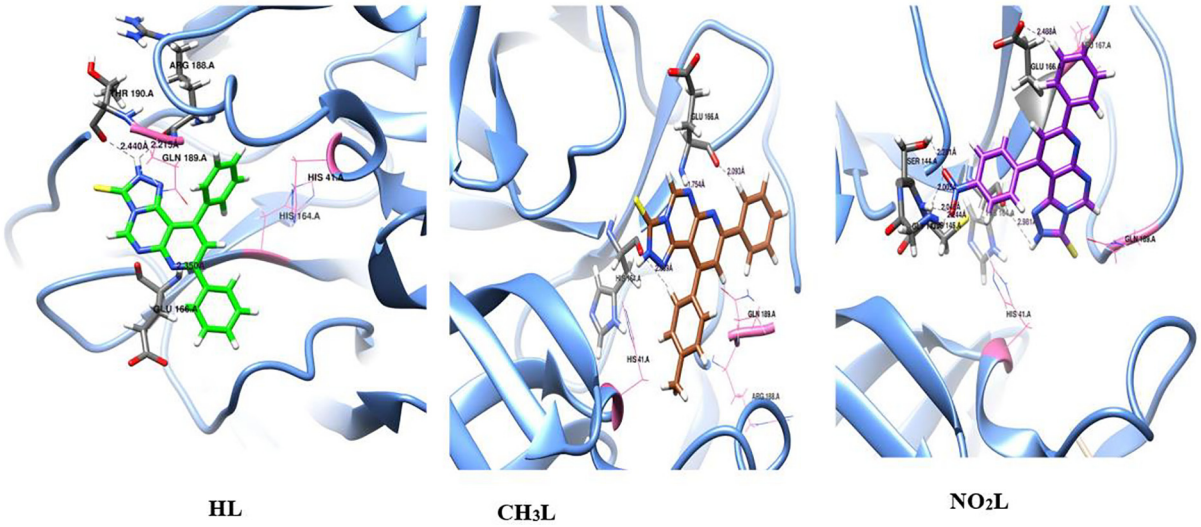

Fig. 10. H-bond and VDW interactions between the surrounded amino acids of M^{pro} receptor (PDB :6WTT) and the heterocyclic ligand compounds.

Table 4
Binding affinity between the optimized ligands and M^{pro} enzyme of SARS CoV-2 with 7JRN.

Compound Name	Binding affinity (fitness)	Protein residue name	Compound residue name	H-Bond length (Å)	Bond energy (kcal/mol)	Protein residue name	VDW Energy (kcal/mol)
HL	−113.5	GLU-166.A	N	2.350	−5.242	HIS-41.A	−6.281
		ARG-188.A	O	2.215	−7.000	HIS-164.A	−4.972
		THR-190.A	O	2.440	−2.851	GLN-189.A	−10.762
CH_3L	−105.2	HIS-164.A	HC	2.839	−4.255	HIS-41.A	−6.692
		GLU-166.A	HC	2.093	−6.692	ARG-188.A	−12.187
			N	1.754		GLN-189.A	−7.916
NO_2L	−128.6	GLY-143.A	O	2.244	−3.500	HIS-41.A	−4.754
		SER-144.A	O	2.281	−7.995	LEU-167.A	−4.271
		CYS-145.A	O	2.046	−9.500	GLN-189.A	−8.121
			O	2.005	−6.210		
		HIS-164.A	HN	2.981	−6.474		
		GLU-166.A	HC	2.488	−3.343		

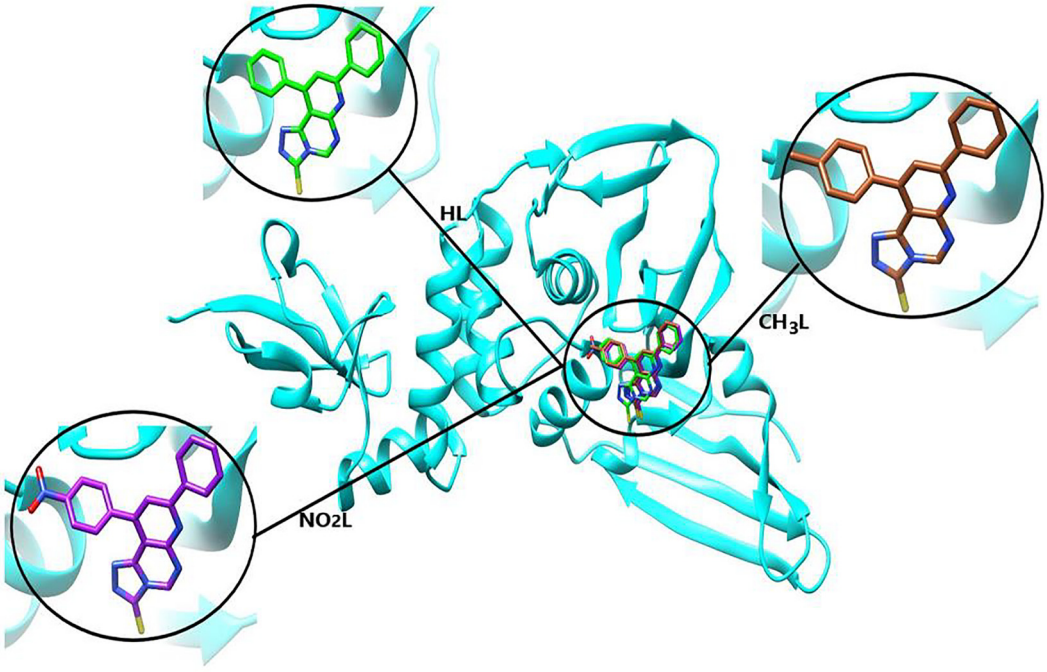

Fig. 11. Molecular docking of studied ligands, **HL**, **CH_3L** and **NO_2L** with PL^{pro} enzyme (PDB :7JRN).

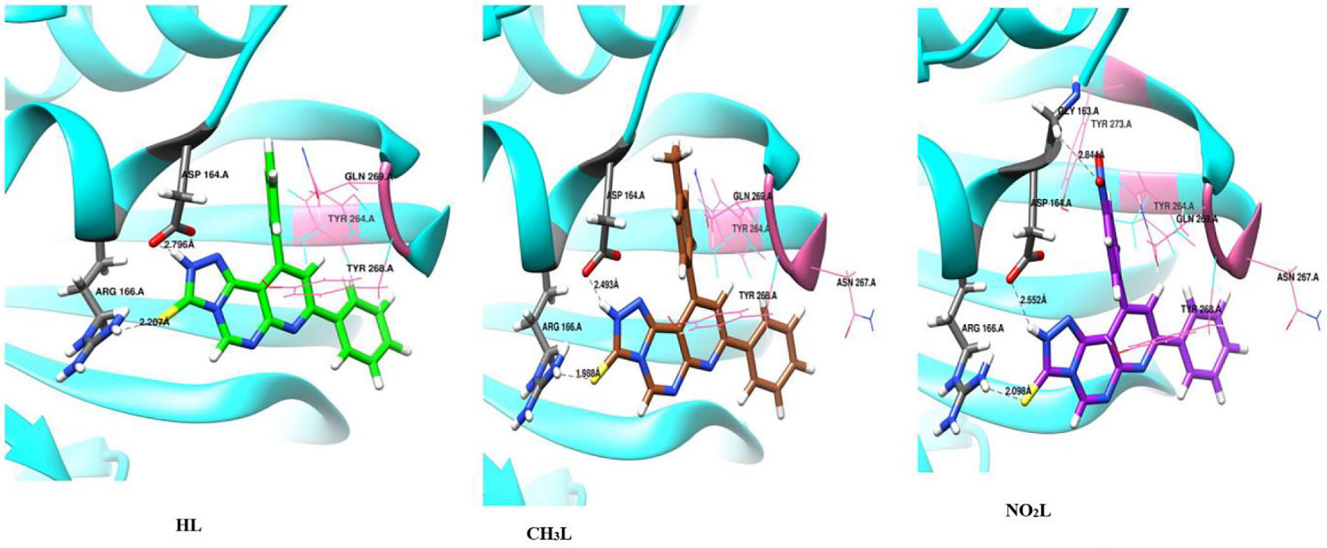

Fig. 12. H-bond interactions between the surrounded amino acids of PL^{pro} receptor (PDB :7JRN) and the heterocyclic ligand compounds.

Table 5
Binding affinity between the optimized ligands and PL^{pro} enzyme of SARS CoV-2 with 7JRN.

Compound Name	Binding affinity (fitness)	Protein residue name	Compound residue name	H-Bond length (Å)	Bond energy (kcal/mol)	Protein residue name	VDW Energy (kcal/mol)
HL		ASP-164.A	HN	2.796	−7.336	TYR-264.A	−13.628
		ARG-166.A	S	2.207	−4.194	TYR-268.A	−18.029
	−100.3					GLN-269.A	−6.064
CH_3L	−102.8	ASP-164.A	HN	2.493	−6.15	TYR-264.A	−14.249
		ARG-166.A	S	1.988	−8.18	ASN-267.A	−4.6208
						TYR-268.A	−18.118
						GLN-269.A	−7.142
NO_2L		GLY-163.A	O	2.844	−3.467	TYR-264.A	−14.578
		ASP-164.A	HN	2.552	−7.718	ASN-267.A	−4.069
	−107.6	ARG-166.A	S	2.098	−6.533	TYR-268.A	−16.955
						GLN-269.A	−7.008
						TYR-273.A	−4.521

4. Conclusion

A previously synthesized heterocyclic compounds 8,10-diphenylpyrido[3,2–e1,2,4]triazolo[4,3–c]pyrimidine-3(2H)-thione derivatives were studied applying DFT and theoretical calculations were performed in this study. In most cases, spectroscopic analyses showed slightly a good matching between theoretical and experimental data reported previously. Electronic properties and reactivity were discussed and it was found that **NO_2L** acts as stronger nucleophile than the other ligands through its nitro group. The studied compounds theoretically proved to be active towards chemical reactions through the small energy gap. NCI-RDG analysis revealed presence of Van der Waals interaction and also strong repulsion interaction inside the aromatic rings. Prediction the biological activity of these compounds was illustrated by performing molecular docking of the optimized molecules with the target of protease enzymes in SARS-CoV-2 viral protein. The docking summarized in studying the interaction with two types of protease enzymes (M^{pro} with PDB 6WTT and PL^{pro} with PDB 7JRN) and the docking results evaluate the strong inhibition effect of **NO_2L** which contains nitro group that increases the possibility to form a strong H-bonds with the amino acid of viral protein.

Funding

No funding for this article.

Declaration of Competing Interest

The authors declare that they have no known competing financial interests or personal relationships that could have appeared to influence the work reported in this paper.

References

[1] S.K. El saedany, M. A. Zein, E.M. Abdelrehim, R.M. Keshk, Synthesis, Anti-Microbial, and Cytotoxic Activities Evaluation of Some New Pyrido[2,3-d] Pyrimidines, J.Hetrocyclic Chem. 53 (2016) 1534. https://doi.org/10.1002/jhet.2460.
[2] E.M. Abdelrehim, M.A. Zein, Synthesis of Some Novel Pyrido[2,3-*d*]pyrimidine and Pyrido[3,2-*e*][1,3,4]triazolo and Tetrazolo[1,5-*c*]pyrimidine Derivatives as Potential Antimicrobial and Anticancer Agents, J. Hetrocyclic Chem. 55 (2018) 419, https://doi.org/10.1002/jhet.3058.
[3] C. Kurumurthy, P. Sambasiva, B. Veeraswamy, G. Santhoshkumar, P. Shanthan, B. Narsaiah, L.R. Velatooru, R. Pamanji, R. Venkateswara, Synthesis of novel alkyltriazole tagged pyrido[2,3-d]pyrimidine derivatives and their anticancer activity, Eur. J. Med. Chem. 46 (2011) 3462–3468.
[4] D.D. Boehr, A.R. Farley, G.D. Wright, J.R. Cox, Analysis of the π-π Stacking Interactions between the Aminoglycoside Antibiotic Kinase APH(3′)-IIIa and Its

Nucleotide Ligands, Chem. Biol. 9 (2002) 1209, https://doi.org/10.1016/S1074-5521(02)00245-4.
[5] T.V. Pyrkov, D.V. Pyrkova, E.D. Balitskaya, R.G. Efremov, The role of stacking interactions in complexes of proteins with adenine and guanine fragments of ligands, Acta Nat. 1 (2009) 124.
[6] S.K. Panigrahi, G.R. Desiraju, Strong and weak hydrogen bonds in the protein–ligand interface, Proteins 67 (2007) 128, https://doi.org/10.1002/prot.21253.
[7] M. A. Williams, J. E. Ladbury, Hydrogen Bonds in Protein– Ligand Complexes (Eds: H.-J.Bohm, G. Schneider), FRG: WileyVCH Verlag GmbH & Co. KGaA, Weinheim (2003) 137-161
[8] R.G. Efremov, A.O. Chugunov, T.V. Pyrkov, J.P. Priestle, A.S. Arseniev, E. Jacoby, Molecular docking: The role of noncovalent interactions in the formation of protein-nucleotide and protein-peptide complexes, Curr. Med. Chem. 14 (2007) 393.
[9] A.M. Gallina, P. Bork, D. Bordo, Hydrocarbon binding by proteins: structures of protein binding sites for ≥C10 linear alkanes or long-chain alkyl and alkenyl groups, J. Mol. Recognit. 27 (2014) 65, https://doi.org/10.1021/jo502488e.
[10] N.S. Scrutton, A.R. Raine, Biochem, Cation-pi bonding and amino-aromatic interactions in the biomolecular recognition of substituted ammonium ligands, J. 1 (1996) 319.
[11] R. Wu, T.B. McMahon, Investigation of Cation-π Interactions in Biological Systems, J. Am. Chem. Soc. 130 (2008) 12554.
[12] Y. Lu, Y. Wang, W. Zhu, Nonbonding interactions of organic halogens in biological systems: implications for drug discovery and biomolecular design, Phys. Chem. 12 (2010) 4543, https://doi.org/10.1039/B926326H.
[13] P. Zhou, F. Tian, J. Zou, Z. Shang, Rediscovery of halogen bonds in protein-ligand complexes, Mini Rev. Med. Chem. 10 (2010) 309, https://doi.org/10.2174/138955710791331016.
[14] P. Kukic, J.E. Nielsen, Electrostatics in proteins and protein-ligand complexes, Future Med. Chem. 2 (2010) 647, https://doi.org/10.4155/fmc.10.6.
[15] M. T. Neves-Petersen, S. B. Petersen, Biotechnol. Protein electrostatics: A review of the equations and methods used to model electrostatic equations in biomolecules - Applications in biotechnology, Annu. Rev. 9 (2003) 315. DOI: 10.1016/S1387-2656(03)09010-0.
[16] P. Zhou, J. Huang, F. Tian, Specific noncovalent interactions at protein-ligand interface: implications for rational drug design, Curr. Med. Chem. 19 (2012) 226, https://doi.org/10.2174/092986712803414150.
[17] K. Chen, L. Kurgan, Investigation of Atomic Level Patterns in Protein—Small Ligand InteractionsPLoS ONE 4 (2009) 4473. https://doi.org/10.1371/journal.pone.0004473
[18] M. Egli, R.V. Gessner, Proc. Natl. Acad. Stereoelectronic effects of deoxyribose O4' on DNA conformation, Sci. U.S.A. 92 (1995) 180–184. DOI: 10.1073/pnas.92.1.180.
[19] J.J.V. Eynde, D. Fromont, Bull. Soc. Chim. Belg. 106 (1997) 393–397.
[20] J. Sitkowski, L. Stefaniak, T. Dziembowska, E. Grech, E. Jagodzinska, G.A. Webb, J. Molecular Structure 381 (1996) 177–180.
[21] K. Tanaka, K. Nomura, H. Oda, S. Yoshida, K. Mitsuhashi, J. Heterocyclic Chem (1991) 907–911.
[22] L. Kang, L. Zhao, S. Yao, C. Duan, A new architecture of super-hydrophilic β-SiAlON/graphene oxide ceramic membrane for enhanced anti-fouling and separation of water/oil emulsion, Ceram. Int. 45 (2019) 16717.
[23] Y. Yang, L. Kang, H. Li, Enhancement of photocatalytic hydrogen production of BiFeO3 by Gd3+ doping, Ceram. Int. 45 (6) (2019) 8017–8022.
[24] Serpil Kaya, Sultan Erkan, Duran Karakaş, Computational investigation of molecular structures, spectroscopic properties and antitumor-antibacterial activities of some Schiff bases, Spectrochim, Acta Part A: Molecular and Biomolecular Spectroscopy 244 (2021), https://doi.org/10.1016/j.saa.2020.118829 118829.
[25] E.M. Abdelrehim, D.S. El-Sayed, A new synthesis of poly heterocyclic compounds containing [1, 2, 4] triazolo and [1, 2, 3, 4] tetrazolo moieties and their DFT study as expected anti-cancer reagents, Curr. Org. Synth. 17 (2020) 211–223, https://doi.org/10.2174/1570179417666200226092516.
[26] P.J. Stephens, N. Harada, ECD cotton effect approximated by the Gaussian curve and other methods, Chirality 22 (2009) 229, https://doi.org/10.1002/chir.20733.
[27] M. J. Frisch, et al; Gaussian 09, Revision A.02, Gaussian, Inc., Wallingford CT, (2016).
[28] A.D. Becke, A new mixing of Hartree-Fock and local density-functional theories, J. Chem. Phys. 98 (1993) 5648, https://doi.org/10.1063/1.464304.
[29] M. Frisch, G. Trucks, H. Schlegel, G. Scuseria, M. Robb, J. Cheeseman, J. Montgomery, T. Vreven, K. Kudin, J. Burant, Inc (2003).
[30] Ş. Güveli, N. Özdemir, T. Bal-Demirci, B. Ülküseven, M. Dinçer, Ö. Andaç, Quantum chemical, spectroscopic and X-ray diffraction studies on nickel complex of 2-hydroxyacetophenone thiosemicarbazone with triphenylphospine, Polyhedron 29 (12) (2010) 2393–2403, https://doi.org/10.1016/j.poly.2010.05.004.
[31] R. Dennington, T.A. Keith, J.M. Millam, GaussView, Version 6.1, Semichem Inc., Shawnee Mission, KS, 2016.
[32] G. Zhurko, D. Zhurko, ChemCraft 1.8 http://www.chemcraftprog.com 2005.
[33] D. Guillaumont, S. Nakamura, Calculation of the absorption wavelength of dyes using time-dependent density-functional theory (TD-DFT), Dyes Pigments 46 (2) (2000) 85–92, https://doi.org/10.1016/S0143-7208(00)00030-9.
[34] Y.F. Chen, Y.J. Chen, J.M. Yang, GEMDOCK: An Integrated Environment for Computer-aided Drug Design and Its Applications, (2007).
[35] E.F. Pettersen, T.D. Goddard, C.C. Huang, G.S. Couch, D.M. Greenblatt, E.C. Meng, T.E. Ferrin, UCSF Chimera—A Visualization System for Exploratory Research and Analysis, J. Comput. Chem. 25 (2004) 1605.
[36] C.P. Kaushik, Krishan Kumar, S.K. Singh, Dharmendra Singh, Sangita Saini, Synthesis and antimicrobial evaluation of 1,4-disubstituted 1,2,3-triazoles with aromatic ester functionality, Arabian Journal of Chemistry,Volume 9 (6) (2016) 865-871 1878-5352, https://doi.org/10.1016/j.arabjc.2013.09.023.
[37] P. Geerlings, F. De Proft, Chemical Reactivity as Described by Quantum Chemical Methods, Int. J. Mol. Sci. 3 (4) (2002) 276–309, https://doi.org/10.3390/i3040276.
[38] N.S. Venkataramanan, A. Suvitha, Y. Kawazoe, J. Mol. Liq. 260 (2018) 18, https://doi.org/10.1016/j.molliq.2018.03.071.
[39] G. Krishna, V.S. Pillai, M.V. Veettil, Approaches and advances in the development of potential therapeutic targets and antiviral agents for the management of SARS-CoV-2 infection, Eur. J. Pharmacol. 885 (2020), https://doi.org/10.1016/j.ejphar.2020.173450 173450.
[40] C.A. Omolo, N. Soni, V.O. Fasiku, I. Mackraj, T. Govender, Update on therapeutic approaches and emerging therapies for SARS-CoV-2 virus, Eur. J. Pharmacol. 883 (2020), https://doi.org/10.1016/j.ejphar.2020.173348 173348.